

Elliptic Flow from a Transversally Thermalized Fireball

U. Heinz and S.M.H. Wong

Physics Department, The Ohio State University, Columbus, OH 43210

(Dated: October 25, 2018)

The agreement of elliptic flow data at RHIC at central rapidity with the hydrodynamic model has led to the conclusion of very rapid thermalization. This conclusion is based on the intuitive argument that hydrodynamics, which assumes instantaneous local thermalization, produces the largest possible elliptic flow values and that the data seem to saturate this limit. We here investigate the question whether incompletely thermalized viscous systems may actually produce more elliptic flow than ideal hydrodynamics. Motivated by the extremely fast primordial longitudinal expansion of the reaction zone, we investigate a toy model which exhibits thermalization only in the transverse directions but undergoes collisionless free-streaming expansion in the longitudinal direction. For collisions at RHIC energies, elliptic flow results from the model are compared with those from hydrodynamics. With the final particle yield and k_{\perp} -distribution fixed, the transversally thermalized model is shown not to be able to produce the measured amount of elliptic flow. This investigation provides further support for very rapid local kinetic equilibration at RHIC. It also yields interesting novel results for the elliptic flow of massless particles such as direct photons.

PACS numbers: 25.75.-q, 24.10.Nz, 25.75.Ld, 24.85.+p

I. INTRODUCTION

Recently the STAR collaboration showed [1, 2, 3] that the k_{\perp} and centrality dependence of the measured elliptic flow coefficient v_2 of pions and protons at the Relativistic Heavy Ion Collider (RHIC) largely agreed with those generated from the hydrodynamic model simulation of heavy ion collisions [4, 5, 6, 7]. This was subsequently confirmed by data from the PHENIX [8] and PHOBOS [9] collaborations. v_2 is the second coefficient of an azimuthal Fourier expansion of the transverse momentum spectrum around the beam axis [10] and, for collisions between identical nuclei, is the lowest non-zero anisotropic flow coefficient at midrapidity. Given that the main prerequisite of the hydrodynamic model is complete local thermal equilibrium, which requires very intense rescattering among the matter constituents, it was argued that hydrodynamics should give the largest possible elliptic flow, and the observation that the data saturate the hydrodynamic limit was taken as evidence that thermalization must be very fast at RHIC for central and semi-central collisions [6, 7, 11].

Elliptic flow *requires* reinteractions within the produced matter as a mechanism for transferring the initial spatial deformation of the reaction zone in non-central collisions onto momentum space. It is thus plausible to expect that the largest elliptic flow signal is produced in the hydrodynamic limit, i.e. in the limit of infinite rescattering rates [6, 7, 11]; however, a proof for this hypothesis has not yet been found. In hydrodynamics, collective flow is generated by pressure gradients, and flow anisotropies such as elliptic flow require anisotropic pressure gradients in the plane transverse to the beam direction. The longitudinal pressure plays a less visible role: the work done by the longitudinal pressure reduces the transverse energy dE_T/dy and thereby, for given initial conditions

for the energy density deposited in the reaction zone, the amount of transverse flow at freeze-out. If there were no longitudinal pressure, more of the initially deposited energy would go into the transverse directions, leading to flatter transverse momentum spectra. It is, at least in principle, conceivable that this could also lead, at fixed radial flow, to larger anisotropies of the transverse collective flow. If this were indeed the case and, at fixed slope of the angle-averaged spectra, larger values of v_2 could be generated in this way than within the usual hydrodynamic, the early thermalization argument would break down since the RHIC data [1, 2, 3] would no longer saturate the theoretical prediction from such a model.

To explore this hypothetical possibility, we study in this paper a toy model which assumes that, at high collision energies, during the earliest collision stages the longitudinal momenta of the produced particles do not thermalize, but that the strong initial longitudinal expansion is instead dominated by collisionless free-streaming. The initial transverse momenta are much smaller and assumed to thermalize quickly. This results in a system with local transverse, but zero longitudinal pressure. Due to the masslessness of the partons created in the reaction zone the trace of the energy momentum tensor vanishes; in the absence of longitudinal pressure P_{\parallel} , the transverse pressure P_{\perp} must thus be related to the initial energy density $\varepsilon = T^{00}$ by $\varepsilon = 2P_{\perp}$ (instead of the usual $\varepsilon = 3P$). This results in a much stiffer equation of state for the transverse dynamics (see Sec. II B), giving more flow and possibly stronger flow anisotropies. Of course, if the transverse momenta thermalize, the longitudinal momenta should do so eventually, too. We assume in our model that when this happens the flow anisotropies have already almost reached their asymptotic values [12].

Similar to the hydrodynamic simulations [4, 5, 6, 7], we assume that the longitudinal free-streaming dynam-

ics is boost invariant [14] and correspondingly concentrate on the central rapidity region. Starting from a kinetic description of the longitudinally free-streaming but transversally thermalized gluonic system (which we call “transversally thermalized model”, TTHM), we derive a set of macroscopic evolution equations (TTHM equations) which we solve with appropriate initial conditions. The impact parameter dependence of the initial conditions is handled in the same way as in the hydrodynamic simulations. When comparing our TTHM solutions to those from the ideal hydrodynamic model (HDM) we retune the initial conditions in such a way that for central collisions ($b = 0$ fm) roughly the same multiplicities and spectral slopes at midrapidity are obtained. We then compare the momentum-space anisotropy v_2 in the two approaches, as a function of transverse momentum k_\perp and impact parameter b .

II. CONSTRUCTING A TRANSVERSALLY THERMALIZED SYSTEM

A. The Phase-Space Distribution Function

We consider a gluon dominated system at a short time after nuclear contact. We assume that at that time the transverse gluon momenta are already thermalized but that the system is still free-streaming along the beam direction. The system is required to possess longitudinal boost invariance, reflecting a boost invariant primary particle production mechanism [14]. For easiest implementation we assume that the collision energy is so high that the colliding nuclei are Lorentz contracted to two infinitesimally thin sheets in the z -direction and that all produced particles point back to $z = t = 0$. Their longitudinal momenta and coordinates thus satisfy $z = u_z t$ or $k_0 z = k_z t$ where $u_z = k_z/k_0$. This automatically identifies [14] the rapidity

$$y = \frac{1}{2} \ln \left(\frac{k_0 + k_z}{k_0 - k_z} \right) \quad (2.1)$$

of the produced particles with their spacetime rapidity

$$\eta = \frac{1}{2} \ln \left(\frac{t + z}{t - z} \right). \quad (2.2)$$

We thus make the ansatz

$$f(\mathbf{k}, \mathbf{x}, t) = \delta(k_0 z - k_z t) \tilde{h}(\mathbf{k}, \mathbf{x}, t). \quad (2.3)$$

Longitudinal free-streaming is implemented by the condition

$$\left(k_0 \frac{\partial}{\partial t} + k_z \frac{\partial}{\partial z} \right) f(\mathbf{k}, \mathbf{x}, t) = 0. \quad (2.4)$$

Since the δ -function factor solves this equation trivially, this implies a constraint for \tilde{h} . The latter is most conveniently expressed by using an alternate coordinate system (we hereafter make explicit use of the masslessness

of the produced gluon degrees of freedom, by setting $m_\perp = \sqrt{m^2 + k_\perp^2} \rightarrow k_\perp$):

$$t = \tau \cosh \eta, \quad z = \tau \sinh \eta, \quad (2.5)$$

$$k_0 = k_\perp \cosh y, \quad k_z = k_\perp \sinh y. \quad (2.6)$$

In these coordinates the ansatz Eq. (2.3) becomes

$$f(\mathbf{k}, \mathbf{x}, t) = \frac{\delta(\eta - y)}{k_\perp \tau \cosh(\eta - y)} \tilde{h}(\mathbf{k}_\perp, \mathbf{x}_\perp, \eta - y, \tau) \quad (2.7)$$

where the dependence of \tilde{h} on only \mathbf{k}_\perp and the difference $\eta - y$ results from the requirement of longitudinal boost invariance. We implement transverse thermalization by the ansatz

$$\tilde{h}(\mathbf{k}_\perp, \mathbf{x}_\perp, \eta - y, \tau) = \frac{\tau_0 k_\perp}{\gamma_\perp} \cosh(\eta - y) \frac{1}{e^{k \cdot u/T} - 1}, \quad (2.8)$$

where $u^\mu = \gamma_\perp (\cosh \eta, \mathbf{v}_\perp, \sinh \eta)$ is the flow vector with Bjorken longitudinal flow velocity $v_z = \tanh \eta$ [14] and transverse flow velocity $\mathbf{v}_\perp = \mathbf{v}_\perp(\mathbf{x}_\perp, \tau)$ ($\gamma_\perp^{-1} = \sqrt{1 - v_\perp^2}$). $T = T(\mathbf{x}_\perp, \tau)$ is the temperature characterizing the thermalized transverse momentum spectrum. In the local rest frame T is a function of the rest frame coordinates \mathbf{x}_\perp^* and $\tau^* = t^*$ which after the standard [15] successive transverse and longitudinal boosts to the laboratory frame, with \mathbf{v}_\perp and $v_z = \tanh \eta$ respectively, are related to the laboratory variables by

$$\begin{aligned} t^* &= \gamma_\perp (t \cosh \eta - z \sinh \eta - \mathbf{v}_\perp \cdot \mathbf{x}_\perp) \\ &= \gamma_\perp (\tau - \mathbf{v}_\perp \cdot \mathbf{x}_\perp) = u \cdot x \end{aligned} \quad (2.9)$$

$$\begin{aligned} x_{\perp\parallel}^* &= \gamma_\perp (x_{\perp\parallel} - v_\perp (t \cosh \eta - z \sinh \eta)) \\ &= \gamma_\perp (x_{\perp\parallel} - v_\perp \tau) = -m \cdot x \end{aligned} \quad (2.10)$$

$$x_{\perp\perp}^* = x_{\perp\perp}. \quad (2.11)$$

The additional \parallel and \perp subscripts denote the components of \mathbf{x}_\perp parallel and perpendicular to \mathbf{v}_\perp , respectively, and the vector m^μ is defined in Eq. (2.16) below. The sequence of boosts described here agrees with the standard choice [15] and gives the simplest structure for the set of 4-vectors needed for decomposition of the energy momentum tensor (see Sec. II B). As one can see from Eqs. (2.9)-(2.11), the dependence of T on \mathbf{x}_\perp^* and t^* in the local rest frame translates into a dependence on \mathbf{x}_\perp and τ in the laboratory frame.

By virtue of the factor $\delta(\eta - y)$, the argument of the Bose distribution in Eq. (2.8) reduces in the local rest frame to $k \cdot u = k_\perp$, showing explicitly that the system is only transversally thermalized. Combining Eqs. (2.7) and (2.8) and exploiting the δ -function, the distribution function simplifies to

$$\begin{aligned} f(\mathbf{k}, \mathbf{x}, t) &= \frac{\tau_0}{\tau} \delta(\eta - y) h(\mathbf{k}_\perp, \mathbf{x}_\perp, t), \\ h(\mathbf{k}_\perp, \mathbf{x}_\perp, t) &= \frac{1}{\gamma_\perp} \frac{1}{e^{k \cdot u/T} - 1}. \end{aligned} \quad (2.12)$$

In the new coordinates, f satisfies the relativistic transport equation

$$\left(k_{\perp} \cosh(\eta-y) \frac{\partial}{\partial \tau} - \frac{k_{\perp}}{\tau} \sinh(\eta-y) \frac{\partial}{\partial \eta} + \mathbf{k}_{\perp} \cdot \nabla_{\perp} \right) f(\mathbf{k}, \mathbf{x}, t) = \mathcal{C}(\mathbf{k}, \mathbf{x}, t), \quad (2.13)$$

where the collision term \mathcal{C} is responsible for keeping the transverse momenta thermalized while not changing any of the longitudinal momenta. Due to the implemented free-streaming properties we have

$$\left(\cosh(\eta-y) \frac{\partial}{\partial \tau} - \sinh(\eta-y) \frac{1}{\tau} \frac{\partial}{\partial \eta} \right) \left(\frac{\tau}{\tau_0} \delta(\eta-y) \right) = 0$$

such that Eq. (2.13) reduces to the following kinetic equation for the transverse distribution function:

$$\left(k_{\perp} \frac{\partial}{\partial \tau} + \mathbf{k}_{\perp} \cdot \nabla_{\perp} \right) h(\mathbf{k}_{\perp}, \mathbf{x}_{\perp}, \tau) = \mathcal{C}(\mathbf{k}, \mathbf{x}, t). \quad (2.14)$$

The space-time evolution of $h(\mathbf{k}_{\perp}, \mathbf{x}_{\perp}, \tau)$ is entirely due to the collisions and collective transverse expansion, but decoupled from the boost invariant longitudinal expansion. The collisions must be sufficiently dominant over the transverse expansion to maintain the equilibrium form of $h(\mathbf{k}_{\perp}, \mathbf{x}_{\perp}, \tau)$ given above.

We are aiming at a macroscopic description on the basis of the differential conservation laws for energy and momentum, similar to hydrodynamics. This requires the construction of $T^{\mu\nu}$ from the distribution functions. Due to the different microscopic physics in the longitudinal and transverse directions implemented in our model, there are now more vectors required to construct a complete set of tensors with respect to which $T^{\mu\nu}$ should be decomposed. The set of four-vector fields that we need are

$$\begin{aligned} u^{\mu}(\mathbf{x}_{\perp}, \eta, \tau) &= \gamma_{\perp}(\cosh \eta, \mathbf{v}_{\perp}, \sinh \eta), \\ n^{\mu}(\mathbf{x}_{\perp}, \eta, \tau) &= (\sinh \eta, 0, 0, \cosh \eta), \\ m^{\mu}(\mathbf{x}_{\perp}, \eta, \tau) &= \gamma_{\perp}(v_{\perp} \cosh \eta, \hat{\mathbf{v}}_{\perp}, v_{\perp} \sinh \eta). \end{aligned} \quad (2.15)$$

They arise from the following local rest frame vectors by successive boosts with \mathbf{v}_{\perp} and v_z as described above:

$$\begin{aligned} u^{\mu}(\mathbf{x}_{\perp}, \eta, \tau) &= (1, 0, 0, 0), \\ n^{\mu}(\mathbf{x}_{\perp}, \eta, \tau) &= (0, 0, 0, 1), \\ m^{\mu}(\mathbf{x}_{\perp}, \eta, \tau) &= (0, \hat{\mathbf{v}}_{\perp}, 0). \end{aligned} \quad (2.16)$$

One is timelike, $u^2 = 1$, while the other two are spacelike, $n^2 = m^2 = -1$. They are mutually orthogonal: $u \cdot n = u \cdot m = n \cdot m = 0$. With these vectors, the distribution can be expressed in a form which is explicitly boost invariant under longitudinal boosts:

$$f(\mathbf{k}, \mathbf{x}, t) = \frac{\tau_0}{\tau} \frac{\delta(k \cdot n) (k \cdot u - v_{\perp} k \cdot m)}{e^{k \cdot u/T} - 1}. \quad (2.17)$$

B. Energy-Momentum Tensor and Conservation Laws

Based on the structure (2.17) for the phase-space distribution function we want to derive a macroscopic set of dynamical equations based on the conservation laws for energy and momentum. In terms of the distribution function f , the energy-momentum tensor is given by

$$T^{\mu\nu}(\mathbf{x}, t) = \nu_g \int \frac{d^3 k}{(2\pi)^3} \frac{k^{\mu} k^{\nu}}{k^0} f(\mathbf{k}, \mathbf{x}, t), \quad (2.18)$$

where $\nu_g = 2 \cdot 8 = 16$ is the degeneracy factor for color and helicity of the gluons. From the previous subsection we know that $f(\mathbf{k}, \mathbf{x}, t)$ depends on the three 4-vectors u^{μ} , n^{μ} and m^{μ} . The most general form of the tensor $T^{\mu\nu}$ thus reads

$$\begin{aligned} T^{\mu\nu} &= A u^{\mu} u^{\nu} + B n^{\mu} n^{\nu} + C m^{\mu} m^{\nu} + D (u^{\mu} n^{\nu} + n^{\mu} u^{\nu}) \\ &\quad + F (u^{\mu} m^{\nu} + m^{\mu} u^{\nu}) + G (n^{\mu} m^{\nu} + m^{\mu} n^{\nu}) + H g^{\mu\nu} \end{aligned} \quad (2.19)$$

Since the gluons are massless, the trace of $T^{\mu\nu}$ vanishes:

$$T^{\mu}_{\mu} = A - B - C + 4H = 0. \quad (2.20)$$

In the local rest frame we have

$$\begin{aligned} T_{00}^* &= A + H = \varepsilon, \\ T_{xx}^* &= T_{yy}^* = -H = P_{\perp}, \\ T_{zz}^* &= B - H = P_z, \end{aligned} \quad (2.21)$$

where ε is the energy density and P_{\perp} and P_z are the transverse and longitudinal pressure, respectively. In a general frame, all the Lorentz scalar coefficients in Eq. (2.19) can be found by contracting $T^{\mu\nu}$ with all pairwise combinations of the 4-vectors u^{μ} , n^{μ} and m^{μ} . We will denote these contractions by $(uTn) \equiv u_{\mu} T^{\mu\nu} n_{\nu}$ etc. The details of this calculation are given in Appendix A) where we find

$$(uTu) = A + H = \frac{\tau_0}{\tau} \nu_g \frac{\pi^2 T^4}{60} = \varepsilon \quad (2.22)$$

$$(uTm) = -F = -\frac{\tau_0}{\tau} \nu_g \frac{\pi^2 T^4}{120} v_{\perp} = -\frac{v_{\perp}}{2} \varepsilon \quad (2.23)$$

$$(mTm) = C - H = \frac{\tau_0}{\tau} \nu_g \frac{\pi^2 T^4}{120} = \frac{1}{2} \varepsilon \quad (2.24)$$

$$(uTn) = -D = 0 \quad (2.25)$$

$$(nTn) = B - H = 0 = P_z \quad (2.26)$$

$$(nTm) = G = 0 \quad (2.27)$$

From this and Eq. (2.21) we see that

$$B = H = -P_{\perp}, \quad A = \varepsilon + P_{\perp}, \quad (2.28)$$

and the tracelessness condition gives

$$\varepsilon + P_{\perp} + P_{\perp} - \frac{1}{2} \varepsilon - 3P_{\perp} = \frac{1}{2} \varepsilon - P_{\perp} = 0. \quad (2.29)$$

Therefore the equation of state is

$$\varepsilon = 2P_{\perp}. \quad (2.30)$$

Combining this with the expression for (mTm) one finds $C = 0$. The expression for the energy momentum tensor is then

$$T^{\mu\nu} = (\varepsilon + P_{\perp})u^{\mu}u^{\nu} - P_{\perp}n^{\mu}n^{\nu} - P_{\perp}g^{\mu\nu} + P_{\perp}v_{\perp}(u^{\mu}m^{\nu} + m^{\mu}u^{\nu}). \quad (2.31)$$

For completeness and later use we also give the expression for the gluon density in the local comoving frame:

$$n_g = u \cdot j = \frac{\tau_0}{\tau} \nu_g \frac{\zeta(3)T^3}{2\pi^2}, \quad (2.32)$$

where $j^{\mu}(x)$ is the gluon number current:

$$j^{\mu}(\mathbf{x}, t) = \nu_g \int \frac{d^3k}{(2\pi)^3} \frac{k^{\mu}}{k^0} f(\mathbf{k}, \mathbf{x}, t). \quad (2.33)$$

We now proceed to derive the macroscopic evolution equations. We first rewrite the conservation laws

$$\partial_{\nu}T^{\mu\nu} = 0 \quad (2.34)$$

in (η, τ) coordinates,

$$\cosh \eta \left(\frac{\partial T^{0\mu}}{\partial \tau} + \frac{1}{\tau} \frac{\partial T^{z\mu}}{\partial \eta} \right) - \sinh \eta \left(\frac{\partial T^{z\mu}}{\partial \tau} + \frac{1}{\tau} \frac{\partial T^{0\mu}}{\partial \eta} \right) + \nabla_{\perp}^i T^{i\mu} = 0, \quad (2.35)$$

where the sum over i goes over the two transverse directions. When writing these out explicitly in terms of ε , P_{\perp} , and the longitudinal and transverse flow velocities, using Eqs. (2.31) and (2.16), one finds that all explicit dependence on η disappears. Boost-invariant initial conditions (i.e. η -independent initial expressions for ε and P_{\perp} and the structure (2.16) for the vectors u^{μ} , n^{μ} , and m^{μ}) are thus preserved by the macroscopic evolution equations.

For the further analysis we can thus concentrate on the dynamics in the central transverse plane at $z = \eta = 0$. There we have

$$u^{\mu} = \gamma_{\perp}(1, \mathbf{v}_{\perp}, 0), \quad \frac{\partial u^{\mu}}{\partial \eta} = \gamma_{\perp}(0, 0, 0, 1), \quad (2.36)$$

$$n^{\mu} = (0, 0, 0, 1), \quad \frac{\partial n^{\mu}}{\partial \eta} = (1, 0, 0, 0), \quad (2.37)$$

$$m^{\mu} = \gamma_{\perp}(v_{\perp}, \hat{\mathbf{v}}_{\perp}, 0), \quad \frac{\partial m^{\mu}}{\partial \eta} = \gamma_{\perp}(0, \hat{\mathbf{v}}_{\perp}, v_{\perp}) \quad (2.38)$$

Using the η -independence of ε and P_{\perp} we find

$$\begin{aligned} \frac{\partial T^{z\mu}}{\partial \eta} &= \gamma_{\perp}^2 (\varepsilon + P_{\perp})(\delta^{0\mu} + v_{\perp}^i \delta^{i\mu}) - P_{\perp} \delta^{0\mu} \\ &\quad + \gamma_{\perp}^2 P_{\perp} (2v_{\perp}^2 \delta^{\mu 0} + (1 + v_{\perp}^2)v_{\perp}^i \delta^{i\mu}) \\ &= T^{00} \delta^{0\mu} + T^{0i} \delta^{i\mu} = T^{0\mu}, \end{aligned} \quad (2.39)$$

and the equations of motion (2.35) at $z = \eta = 0$ reduce to

$$\frac{\partial T^{00}}{\partial \tau} + \frac{T^{00}}{\tau} + \nabla_{\perp}^j T^{j0} = 0, \quad (2.40)$$

$$\frac{\partial T^{0i}}{\partial \tau} + \frac{T^{0i}}{\tau} + \nabla_{\perp}^j T^{ji} = 0. \quad (2.41)$$

Using the equation of state (2.30) to eliminate ε , these three equations completely determine the three unknown functions P_{\perp} and \mathbf{v}_{\perp} . Since gluons possess no conserved charges, no further current conservation laws need to be considered.

III. HYDRODYNAMICS

For later comparison we here shortly review the parallel procedure for ideal hydrodynamics based on a locally fully thermalized phase-space distribution function

$$f(\mathbf{k}, \mathbf{x}, t) = \frac{1}{e^{k \cdot u/T} - 1}. \quad (3.1)$$

In this case the energy-momentum tensor has the ideal fluid decomposition

$$T^{\mu\nu} = (\varepsilon + P)u^{\mu}u^{\nu} - P g^{\mu\nu}, \quad (3.2)$$

and for a longitudinally boost-invariant system u^{μ} has the same form as in Eq. (2.16). The equation of state is in this case

$$\varepsilon = 3P = \nu_g \frac{\pi^2 T^4}{30}, \quad (3.3)$$

and the gluon density in the local rest frame is

$$n_g = \nu_g \frac{\zeta(3)T^3}{\pi^2}. \quad (3.4)$$

Note that the the energy per particle

$$\frac{\varepsilon}{n_g} = \frac{\pi^4}{30\zeta(3)} T \approx 2.7 T \quad (3.5)$$

agrees exactly with the corresponding expression in the TTHM, see Eqs. (2.22),(2.32).

The pressure is now locally isotropic. With longitudinally boost-invariant (η -independent) initial conditions for ε and P the ansatz Eq. (2.16) for the flow velocity is preserved in time by the equations of motion $\partial_{\nu}T^{\mu\nu} = 0$ [14], and the latter become

$$\frac{\partial T^{00}}{\partial \tau} + \frac{T^{00}}{\tau} + \nabla_{\perp}^j T^{j0} = -\frac{P}{\tau} \quad (3.6)$$

$$\frac{\partial T^{0i}}{\partial \tau} + \frac{T^{0i}}{\tau} + \nabla_{\perp}^j T^{ji} = 0. \quad (3.7)$$

The main difference between these hydrodynamical equations and our TTHM toy model equations (2.40) and (2.41) is the pressure term on the right hand side of Eq. (3.6) which is absent in Eq. (2.40). It indicates the longitudinal work done by the isotropic pressure in hydrodynamics; in the transversely thermalized (TTHM) model there is no longitudinal pressure which could do work in the longitudinal direction.

IV. INITIAL CONDITIONS

We consider Au+Au collisions at RHIC energies. The initial energy density distribution in the transverse plane as a function of impact parameter \mathbf{b} is taken to be proportional to the density of binary nucleon collisions in the transverse plane, calculated from the normalized nuclear thickness function:

$$T_A(\mathbf{x}_\perp) = \int \rho_A(\mathbf{x}_\perp, z) dz, \quad \int d^2x_\perp T_A(\mathbf{x}_\perp) = A. \quad (4.1)$$

For the nuclear number density we took the Wood-Saxon parametrization

$$\rho_A(\mathbf{x}_\perp) = \frac{\rho_0}{e^{(r-R_0)/\xi} + 1} \quad (4.2)$$

with $R_0 = 1.14 A^{1/3}$ fm and $\xi = 0.54$ fm. For collisions between nuclei of masses A and B the number of binary nucleon collisions per unit area in the transverse plane is

$$\frac{dN(\mathbf{x}_\perp, \mathbf{b})}{d^2x_\perp} = \sigma_0 T_A(\mathbf{x}_\perp) T_B(\mathbf{b} - \mathbf{x}_\perp), \quad (4.3)$$

where $\sigma_0 = 40$ mb is the total inelastic nucleon-nucleon cross section. We assume that the generated energy density is proportional to this density. We performed two classes of calculations: in the first class we used the same maximum initial energy density as the authors of [6, 7] ($\varepsilon_0 = e_0 \equiv 23.0$ GeV/fm³ for central ($b=0$ fm)) collisions at an initial time $\tau_0 = 0.6$ fm/c) in order to compare the HDM and TTHM results for similar initial conditions. In the second class of simulations we returned the initial conditions in TTHM such that the same multiplicity density dN/dy and the same slope for the transverse momentum spectrum at midrapidity as in HDM is obtained. Both sets of results will be discussed in the next Section.

V. ELLIPTIC FLOW IN A TRANSVERSALLY THERMALIZED SYSTEM

A. Freeze-out prescription

Just as the HDM, our TTHM model describes the time evolution of macroscopic thermodynamic quantities which must be converted to particle spectra before one can compare with experiments. To do so we use the well-known Cooper-Frye prescription [16] which gives the particle spectrum in terms of an integral over the phase-space distribution function along a so-called freeze-out hypersurface $\Sigma(x)$:

$$E \frac{dN}{d^3k} = \frac{dN}{dy k_\perp dk_\perp d\phi} = \frac{\nu_g}{(2\pi)^3} \int_\Sigma k \cdot d^3\Sigma(x) f(x, k). \quad (5.1)$$

$d^3\Sigma_\mu(x)$ is the four-vector integral measure normal to the hypersurface, and in the TTHM case $f(x, k)$ is a transversally thermalized distribution function of the form (2.12),

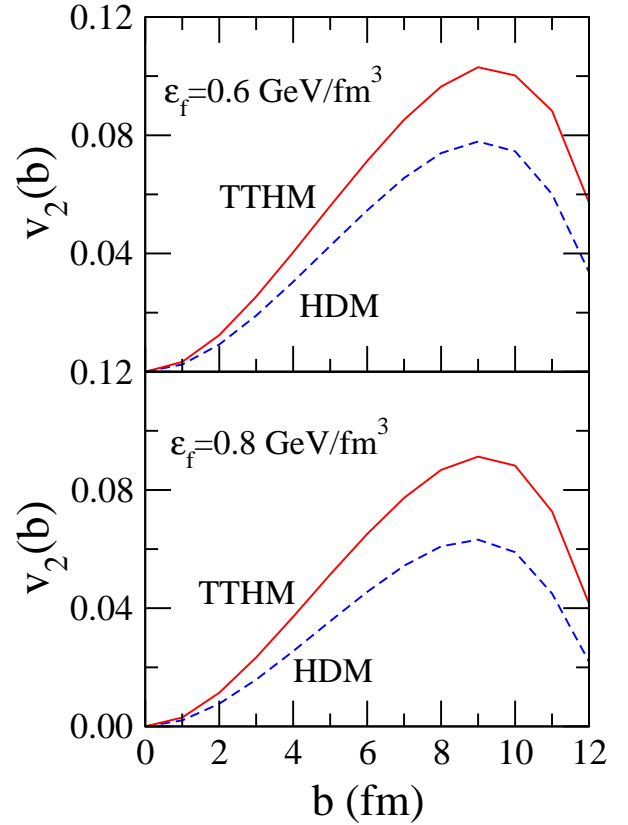


FIG. 1: v_2 as a function of impact parameter at two freeze-out energy densities ε_{f_0} . The solid lines are from our TTHM model while the dashed lines are from hydrodynamic simulations with identical initial conditions.

with flow velocity u^μ evaluated along the freeze-out hypersurface Σ and temperature T calculated via Eq. (2.22) from the energy density on Σ . Longitudinal boost-invariance dictates freeze-out along a surface of fixed longitudinal proper time $\tau_f(\mathbf{x}_\perp)$, and we can write

$$\Sigma_\mu(x) = (\tau_f(\mathbf{x}_\perp) \cosh \eta, \mathbf{x}_\perp, \tau_f(\mathbf{x}_\perp) \sinh \eta). \quad (5.2)$$

This gives

$$k \cdot d^3\Sigma = (k_\perp \cosh(y-\eta) - \mathbf{k}_\perp \cdot \nabla_\perp \tau_f) \tau_f d\eta d^2x_\perp. \quad (5.3)$$

Of course, the η -integration is trivial due to the factor $\delta(\eta-y)$ in the distribution function (2.12).

B. TTHM vs. HDM for identical initial conditions

In Fig. 1 we compare results for the elliptic flow from the TTHM and HDM models for identical initial conditions, taken from [6, 7]. Since the temperature parameter T has a different meaning in our model than usual (only the transverse momenta are thermalized), we enforce “freeze-out” (i.e. we stop the dynamical evolution and calculate the spectra and momentum space

TABLE I: Rapidity densities at $y=0$ and final times τ_f for central collisions with identical initial conditions (see text) in the TTHM and HDM simulations.

ε_f (GeV/fm ³)	TTHM		HDM	
	dN/dy	τ_f (fm/c)	dN/dy	τ_f (fm/c)
0.6	780	6.95	944	5.97
0.8	780	6.48	940	5.36

anisotropies) along a surface of constant energy density ε_f . We show results for two values of this parameter both of which lie in the quark-hadron transition region. Since hadronization certainly involves longitudinal momentum exchange, it will violate our assumption of longitudinal free-streaming, and we should definitely not follow the TTHM dynamics beyond the hadronization point. Of course, by truncating the dynamics at such high freeze-out energy densities we forfeit the possibility of comparing our results directly with experiment. However, a large fraction of the elliptic flow should already have developed at this point [5, 17], and we can still make a meaningful comparison between the hydrodynamic evolution of a fully thermalized quark-gluon plasma and that of a longitudinally free-streaming gluonic system with only transverse thermalization, by comparing the gluon spectra at this common “final” energy density ε_f .

Figure 1 shows v_2 as a function of the impact parameter b . $v_2(b) = \langle \cos(2\phi) \rangle(b)$ is computed from the k_\perp -integrated gluon spectrum at freeze-out as

$$\begin{aligned}
 v_2(b) &= \frac{\int k_\perp dk_\perp d\phi \cos(2\phi) \frac{dN}{dy k_\perp dk_\perp d\phi}(b)}{\int k_\perp dk_\perp d\phi \frac{dN}{dy k_\perp dk_\perp d\phi}(b)} \\
 &= \frac{\int d\phi \cos(2\phi) \frac{dN}{dy d\phi}(b)}{\int d\phi \frac{dN}{dy d\phi}(b)}. \quad (5.4)
 \end{aligned}$$

The Figure shows that, *for identical initial conditions*, the TTHM dynamics generates a *larger* momentum-space asymmetry v_2 than hydrodynamics. We also see that v_2 has not yet fully saturated at these values of ε_f ; the reason for this can be found in Table I which shows that, with the very hard equation of state and initial conditions used here, the above values of ε_f are reached quite early, before the initial spatial deformation has been fully eliminated (see also Fig. 1 in [18]).

The larger values of v_2 from TTHM, however, come also with much flatter transverse momentum spectra, as shown in Fig. 2. Part of this flattening is due to a higher freeze-out temperature in the TTHM. By comparing Eqs. (2.22) and (3.3) one sees at the same energy density ε_f the temperatures in the two models are related by $T_{f,T} = (2\tau_f/\tau_0)^{1/4} T_{f,H}$. With the τ_f values given in Table I, the TTHM freeze-out temperature is about a factor 2 higher than the HDM one. However, the inverse slopes of the spectra shown in Fig. 2 differ by more than this factor 2 (the difference is closer to a factor 2.5-2.6).

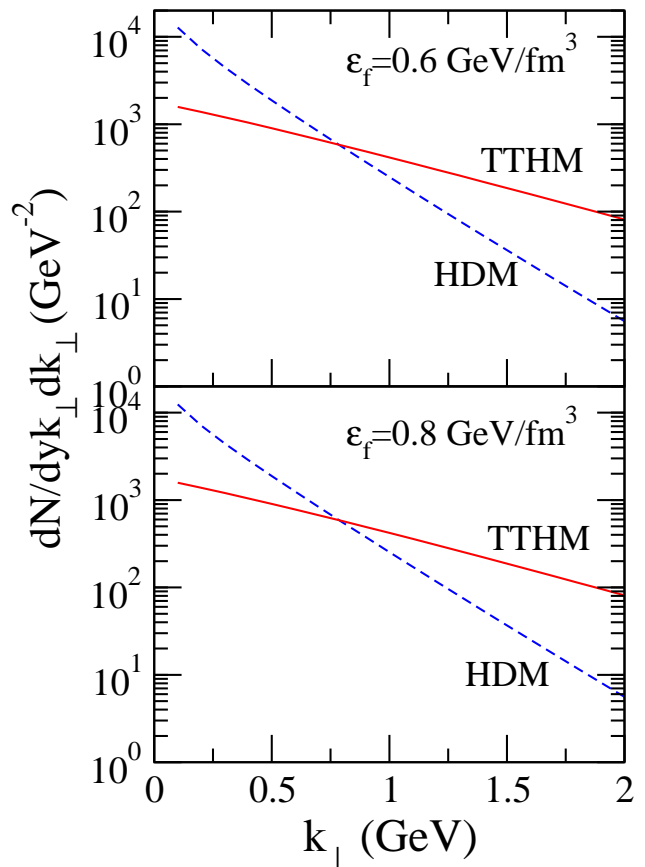


FIG. 2: Gluon k_\perp distribution for central collisions ($b = 0$ fm) and two different values for the freeze-out energy density, for identical initial conditions. The solid lines are for our model while the dashed lines are for hydrodynamics.

This implies that TTHM also creates somewhat stronger radial flow than HDM which, in view of its harder equation of state, is not unexpected.

The initial conditions for the hydrodynamic model (in particular the initial energy density) were tuned [6] to reproduce the measured final multiplicity densities dN_{ch}/dy and spectral slopes in central Au+Au collisions at RHIC; clearly, with these same initial conditions, the transversally thermalized model TTHM will no longer be anywhere close to these data. The larger v_2 values from TTHM in Fig. 1 therefore cannot be compared with the RHIC data, and the comparison with HDM in Fig. 1 is misleading. For a meaningful comparison the initial conditions for TTHM should first be adjusted in such a way that at least the multiplicity densities and spectral slopes for central collisions are similar in both models. This will be our next step.

Before doing so, let us shortly comment on the rapidity densities dN/dy and collision durations listed in Table I. For identical initial conditions, the TTHM gives considerably lower multiplicity densities. This is mostly due to the higher freeze-out temperature in the TTHM which implies that each gluon carries more energy (see

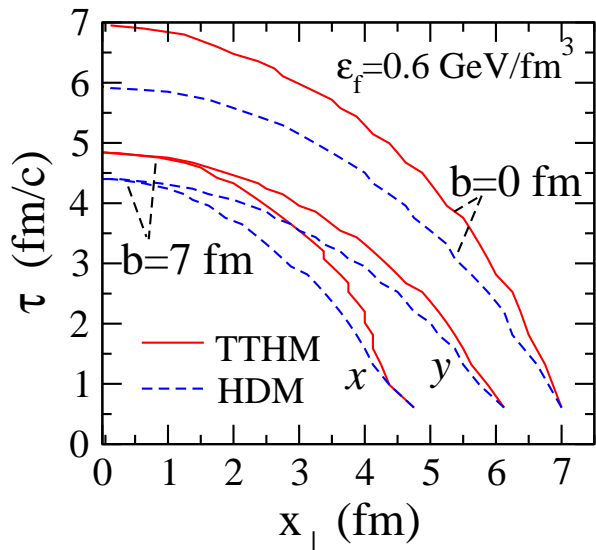


FIG. 3: The freeze-out time $\tau_f(x, y)$ as a function of the transverse coordinates x and y , respectively, for a freeze-out energy density $\epsilon_f = 0.6 \text{ GeV/fm}^3$. The solid (dashed) lines are for TTHM (HDM), respectively. The upper set of curves is for central collisions ($b = 0 \text{ fm}$) where the freeze-out surface is azimuthally symmetric. The lower set of curves corresponds to $b = 7 \text{ fm}$ where we present cuts along the x and y axes, as indicated, to show the spatial azimuthal anisotropy at freeze-out. The impact parameter b points in x direction.

Eq. (3.5)), so the same freeze-out energy density ϵ_f translates into fewer gluons. This argument overestimates the difference between the models, though; the actual difference is smaller since in the HDM the calculation of dN/dy involves an integration over space-time rapidity η which can be interpreted as taking an average over fireballs with different flow rapidities $\eta \neq y$ and correspondingly reduced (redshifted) effective temperatures $T_{\text{eff}} = T_f / \cosh(\eta - y)$.

Longitudinal boost-invariance implies that the total transverse energy per unit rapidity, dE_T/dy , is independent of y . Due to the absence of longitudinal pressure, no longitudinal work is done in the TTHM and dE_T/dy is a constant of motion. This is different from the HDM where work done by the longitudinal pressure reduces dE_T/dy with time. (Both statements were checked numerically.) Table I shows that, within numerical accuracy, the gluon multiplicity per unit rapidity, dN/dy , is also constant in time. While in ideal hydrodynamics (HDM) this is a simple consequence of entropy conservation (for boost-invariant systems dS/dy is a constant of motion [14], and for massless particles the entropy per particle is independent of temperature), there is no such simple reason for this observation in the TTHM which is far from local equilibrium. Detailed checks revealed that, within numerical accuracy, in the TTHM not only the transverse energy per particle, $E_T/N = (dE_T/dy)/(dN/dy)$, but in fact the entire k_\perp -spectrum of the gluons is completely time-independent!

If the system were transversally homogeneous and expanded only longitudinally, this would not be surprising: in the absence of transverse gradients the conservation law Eq. (2.40) for T^{00} simplifies to

$$\frac{\partial(\tau T^{00})}{\partial\tau} = 0 \quad (5.5)$$

with $T^{00} = \epsilon \cosh^2 \eta$. In TTHM a constant product $\epsilon\tau$ implies a constant temperature (see Eq. (2.22)) which, in the absence of transverse flow, then leads to a time-independent transverse momentum spectrum. In our case, however, the system expands in the transverse direction and cools. Our studies show that, in the longitudinal rest frame, the resulting loss in thermal transverse energy per particle is exactly compensated by the gain in transverse collective motion energy, in a way which exactly preserves the shape of the transverse momentum distribution. Although one should think that there must be a simple reason for this intriguing behaviour, we have not been able to find a simple analytical proof and can thus only present the numerical evidence.

The longer freeze-out times in the TTHM simulations (see Table I) are a reflection of the lack of longitudinal pressure. In the HDM the pressure performs longitudinal work and thus causes a more rapid decrease of the energy density with time than in the TTHM. This is further elucidated in Fig. 3 where we show the freeze-out time $\tau_f(x, y)$ as a function of position in the transverse plane. One sees that, for identical initial conditions, the HDM simulations lead to universally earlier freeze-out. This Figure also shows that for non-central Pb+Pb collisions ($b = 7 \text{ fm}$) the source at freeze-out is still larger in the y direction perpendicular to the reaction plane than in the reaction plane; the initial out-of-plane deformation of the reaction zone thus has not yet fully disappeared when the dynamical evolution was stopped. This explains why the elliptic flow had not yet saturated, see Fig. 1 and Fig. 9 below.

C. Retuning the initial conditions for TTHM

Our TTHM model does not include the hadronization of gluons and hence does not allow us to compute hadron spectra; hence we cannot directly compare the gluon multiplicity density dN/dy and their k_\perp -distribution from TTHM at ϵ_f to any data. However, the relation of these quantities to the observable hadron spectra after hadronization is not expected to depend on their dynamical history prior to reaching the “freeze-out” point ϵ_f . Thus, if we want to create TTHM solutions which are likely to lead, after hadronization, to hadron spectra with similar normalization and shape as the data, we can use the gluon rapidity densities and k_\perp -spectra from existing hydrodynamic calculations with initial conditions which were tuned to real data in [6], evaluate them at the same value of ϵ_f where we stop the TTHM evolution, and

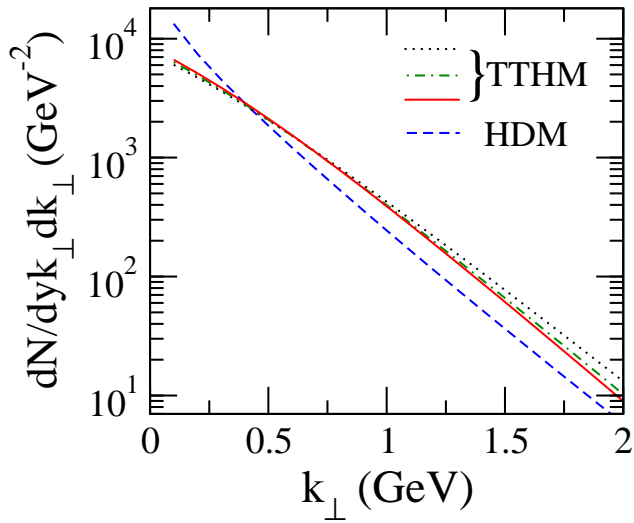


FIG. 4: The gluon k_{\perp} distribution from hydrodynamics (dashed line, with the parameters as given in the text) and TTHM (other lines). The TTHM curves correspond to the following sets of parameters: Dotted line: $\tau_0 = 6$ fm/c, $\varepsilon_0 = e_0/15$; dot-dashed line: $\tau_0 = 7$ fm/c, $\varepsilon_0 = e_0/18$; solid line: $\tau_0 = 7.8$ fm/c, $\varepsilon_0 = e_0/20$. Here $e_0 = 23.0$ GeV/fm³ is the initial central energy density for $b=0$ Au+Au collisions in the HDM.

retune the TTHM initial conditions such that they reproduce these HDM gluon spectra. With the TTHM spectra thus tied down to the final state in central ($b=0$ fm) collisions from the HDM, we can then repeat our comparison of elliptic flow in the two models under more realistic boundary conditions.

For the common decoupling point we chose in both TTHM and HDM the value $\varepsilon_f = 0.35$ GeV/fm³. This may appear somewhat low for still using only gluon degrees of freedom (with an ideal gas EOS in the HDM case), but it has the advantage that then the hydrodynamic model with the ideal massless EOS used here produces an elliptic flow v_2 of roughly the same magnitude as that obtained for pions in Ref. [6] using a more realistic equation of state. Given the good agreement of those HDM calculations with the data [6], we can thus pretend to be comparing directly to data when comparing the TTHM results to our HDM reference.

With this freeze-out energy density, our HDM reference gives the gluon k_{\perp} (or m_{\perp}) spectrum shown in Fig. 4, which integrates to a gluon rapidity density at $y=0$ of $dN/dy \simeq 942$. Given the large difference between the HDM and TTHM spectra for identical initial conditions shown in Fig. 2, it is perhaps not surprising that we found it rather difficult to reproduce the HDM spectrum within the TTHM: one needs to find a way to dramatically lower the radial flow (since the freeze-out temperature is fixed by ε_f and is much higher in TTHM than in HDM) and at the same time increase the normalization of the spectrum in order to raise dN/dy .

There are essentially only three parameters in TTHM

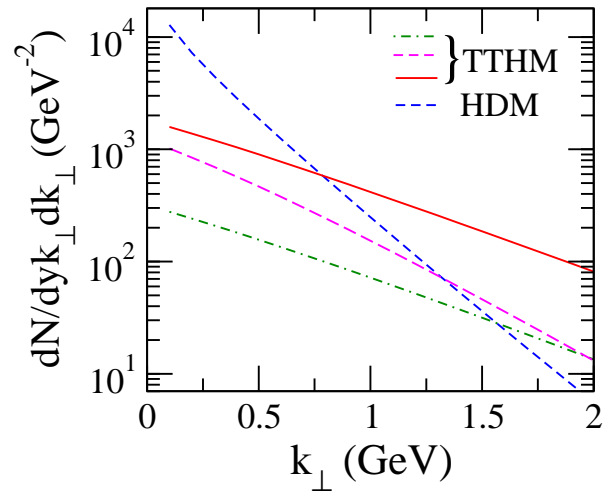


FIG. 5: Variation of the gluon k_{\perp} distribution with various TTHM model parameters. The solid and dashed lines repeat those from Fig. 2 for $\varepsilon_f = 0.6$ GeV/fm³ for comparison. The dot-dashed line is obtained by starting the system earlier at $t_0 = 0.1$ fm/c. The long-dashed line has a lower initial energy density $\varepsilon_i = \varepsilon_0/4$. In each case the remaining parameters are held fixed at the values used in Fig. 2.

that we can play with: ε_0 , τ_0 and ε_f . Examples of the effects of varying them are shown in Fig. 5. The lines from Fig. 2 corresponding to $\varepsilon_f = 0.6$ GeV/fm³ are repeated here for comparison. From Fig. 2 and Table I we learned already that changing ε_f has no influence on dN/dy and little effect on $dN/dyk_{\perp} dk_{\perp}$. This leaves us only with changes of the initial conditions ε_0 and τ_0 . The dot-dashed curve in Fig. 5 shows that decreasing τ_0 from 0.6 to 0.1 fm/c goes in the wrong direction, by reducing dN/dy without having much effect on the slope of the k_{\perp} spectrum. Reducing the initial energy density ε_0 by a factor of four produces the long-dashed line in the figure. Due to the lower initial energy density there is less time until freeze-out to produce radial flow, and the resulting spectrum is steeper, as desired; unfortunately, its normalization dN/dy decreases, too. Combining the insights from these two trial runs, we see that making the TTHM spectrum sufficiently steep requires still much smaller initial energy densities ε_0 , combined with much larger starting times τ_0 for the TTHM transverse dynamical evolution, in order to increase dN/dy . This implies a long transverse thermalization time, which poses intrinsic consistency problems to be addressed later.

Following this route, we find that the HDM gluon spectrum can be roughly reproduced with either one of the following three sets of parameters: $\tau_0 = 6$ fm/c with $\varepsilon_0 = e_0/15$, $\tau_0 = 7$ fm/c and $\varepsilon_0 = e_0/18$, or $\tau_0 = 7.8$ fm/c and $\varepsilon_0 = e_0/20$. The corresponding spectra are shown in Fig. 4. These parameter sets are not unique and the agreement with the HDM spectra is not perfect, but what is clear is that a large reduction of ε_0 by at least 1/15 is essential in TTHM to obtain the much deeper HDM slope.

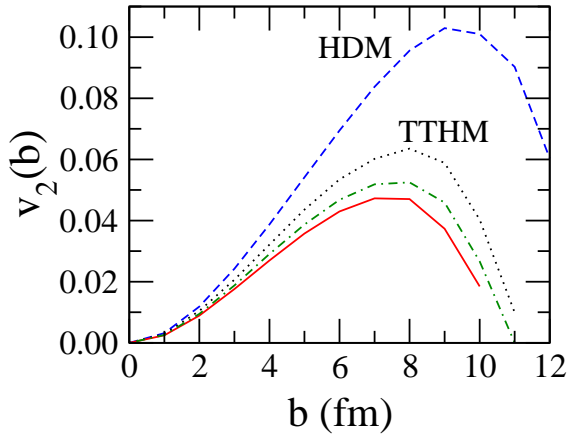


FIG. 6: v_2 as a function of impact parameter from TTHM (solid) and HDM (dashed) simulations tuned to produce identical angle-averaged spectra $dN/dy k_\perp dk_\perp$. The parameters used and notations here are the same as those in Fig. 4.

D. Elliptic flow from TTHM with retuned initial conditions

Figure 6 again shows the impact parameter dependence of v_2 , but now with retuned TTHM initial conditions as described in the previous subsection. With the much lower ε_0 forced upon us by the given slope of the final k_\perp spectrum, there is much less time to generate transverse flow. Figure 6 shows that this leads not only to reduced radial flow, as reflected in the steeper single-particle spectrum for central collisions (see Fig. 4), but also cuts down on the elliptic flow v_2 which now remains significantly below the HDM level. As the latter is representative of the data [3, 11], we conclude that a model with only transversally thermalized momenta in the early collision stages cannot produce as much elliptic flow as required by experiment.

In order to further strengthen this argument let us look at the k_\perp dependence of v_2 and study (see Fig. 7)

$$v_2(k_\perp; b) = \frac{\int d\phi \cos(2\phi) \frac{dN(b)}{dy k_\perp dk_\perp d\phi}}{\int d\phi \frac{dN(b)}{dy k_\perp dk_\perp d\phi}} \quad (5.6)$$

as well as its impact-parameter averaged (“minimum bias” [1]) value (see Fig. 8)

$$v_2(k_\perp) = \frac{\int b db \int d\phi \cos(2\phi) \frac{dN(b)}{dy k_\perp dk_\perp d\phi}}{\int b db \int d\phi \frac{dN(b)}{dy k_\perp dk_\perp d\phi}}. \quad (5.7)$$

We here select for our comparison with HDM one of the above three sets of initial parameters for TTHM, namely $\tau_0 = 7 \text{ fm}/c$ and $\varepsilon_0 = \varepsilon_0/18$, corresponding to the dot-dashed line in Fig. 4.

Figures 7 and 8 show that the k_\perp -slope of v_2 is much lower than in the HDM. This is not only true for the impact parameter averaged elliptic flow shown in Fig. 8, but holds universally for all impact parameters; two examples are plotted in Fig. 7. For $v_2(k_\perp)$ from minimum

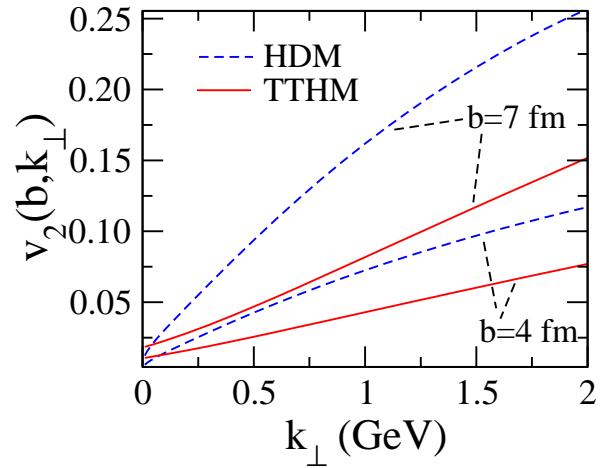


FIG. 7: v_2 as a function of k_\perp for two impact parameters (as indicated) from TTHM (solid) and HDM (dashed) simulations giving identical angle-averaged spectra $dN/dy k_\perp dk_\perp$.

bias events accurate data were published in [1, 2, 3] which follow essentially the dashed HDM line in Fig. 8 and definitely exclude our TTHM.

In Figure 9 we show the time evolution of the momentum anisotropy [5]

$$\varepsilon_p = \frac{\langle T^{xx} - T^{yy} \rangle}{\langle T^{xx} + T^{yy} \rangle} \quad (5.8)$$

where the angular brackets indicate an average over the transverse plane. At freeze-out, this momentum anisotropy is translated into elliptic flow v_2 , where the coefficient between the two variables depends on the particle rest mass [5]. Figure 9 shows that with the hard equation of state for non-interacting massless gluons and RHIC-type initial conditions freeze-out actually happens before the momentum anisotropy saturates [17] (and before the initial spatial anisotropy has fully disappeared). This is even more true for the TTHM (with its even stiffer EOS of $P_\perp = \frac{1}{2}\varepsilon$) than for the HDM (where $P = \frac{1}{3}\varepsilon$): the TTHM freezes out significantly earlier, even though about the same amount of transverse flow is generated.

E. The low- k_\perp limit of $v_2(k_\perp)$ for massless particles

A careful inspection of Figures 7 and 8 shows that at small transverse momenta the shape of the k_\perp -differential elliptic flow $v_2(k_\perp)$ is different for TTHM and HDM. Figure 10 further shows that the small- k_\perp behaviour of the elliptic flow coefficient differs for massive and massless bosons. In Appendix B we present a detailed analytical treatment of the limiting behaviour of $v_2(k_\perp)$ for small transverse momenta. For massive particles, the elliptic flow vanishes quadratically at $k_\perp \rightarrow 0$,

$$v_2(k_\perp) = \mathcal{O}(k_\perp^2) \quad (\text{massive particles}), \quad (5.9)$$

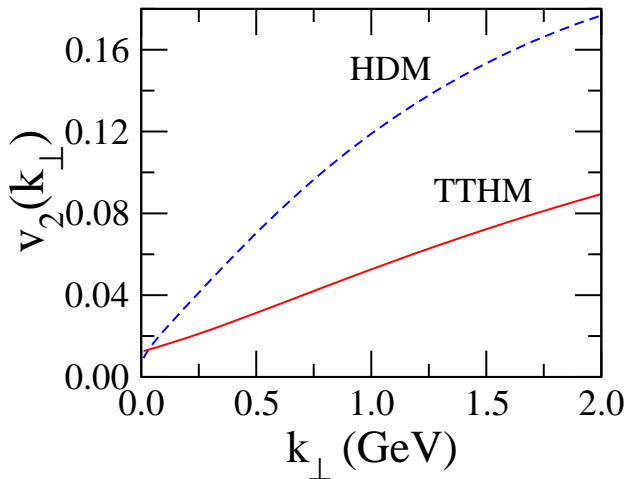


FIG. 8: Impact parameter averaged v_2 as a function of k_\perp from the two models. The dashed line is from HDM, the solid line from TTHM with initial conditions tuned to produce the same angle-averaged transverse momentum spectrum at the same value of ε_f .

going over to an almost linear rise at higher k_\perp (which eventually turns over to saturate at $v_2 = 1$ as $k_\perp \rightarrow \infty$ [7]). The transition from the quadratic rise at low k_\perp to the quasi-linear behaviour at intermediate k_\perp occurs around $k_\perp \sim m$. In detail the transition between these regimes is complex and depends on the ratio m/T of the rest mass to the freeze-out temperature (see Fig. 10): for particles with $m/T < 1$ the elliptic approaches the curve for massless particles while the elliptic flow of heavier particles with $m/T \gg 1$ remains always significantly below that of massless particles.

For massless bosons, the singularity of the Bose distribution at zero momentum leads to a qualitative change in the low-momentum limit of the elliptic flow. For the TTHM, which lacks a thermal spread of the longitudinal momenta, the elliptic flow of massless bosons (gluons or photons) approaches a positive constant with finite positive slope:

$$v_2(k_\perp) = a + bk_\perp + \mathcal{O}(k_\perp^2) \quad (\text{TTHM, massless bosons}). \quad (5.10)$$

In the HDM, the longitudinal thermal momentum smearing weakens the Bose singularity and causes v_2 to still vanish at zero transverse momentum, albeit just barely so: as $k_\perp \rightarrow 0$, $v_2(k_\perp)$ vanishes with infinite slope:

$$v_2(k_\perp) = \frac{\text{const.}}{\ln \frac{T}{k_\perp}} \quad (\text{HDM, massless bosons}). \quad (5.11)$$

It would be interesting to verify this prediction of the hydrodynamic model for photons which are directly emitted from the expanding fireball.

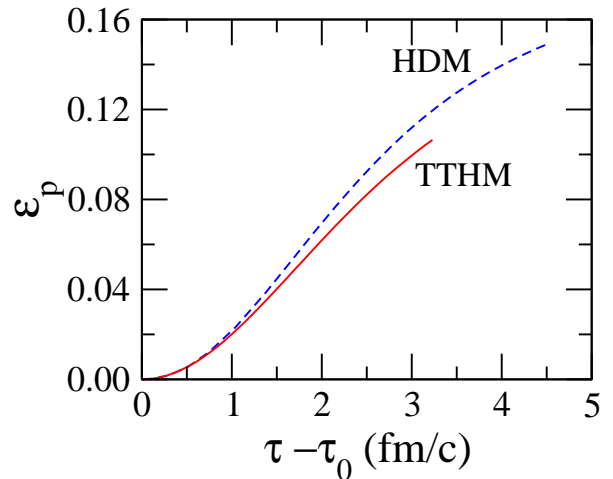


FIG. 9: The asymmetry measure ε_p as a function of the duration of the time evolution at $b = 7$ fm with similar final particle spectra from both models. Again the solid is from TTHM and the dashed line from HDM.

VI. CONCLUSIONS

We have tried to construct a macroscopic dynamical description of the fireball expansion in relativistic heavy-ion collisions which relaxes the usual assumption of complete local thermal equilibrium which underlies the popular and successful hydrodynamical approach. This addresses, on a macroscopic level, the observation that existing parton-based microscopic kinetic models [20, 21, 22] seem unable to generate sufficiently fast thermalization to reach the hydrodynamic limit. We have tested a toy model where transverse momenta are thermalized very quickly while the system is streaming freely in the longitudinal direction (i.e. without longitudinal momentum transfer). The initial longitudinal motion was assumed to be boost-invariant, and the model preserves this property dynamically at later times.

Starting from the kinetic transport equation, we derived the corresponding macroscopic equations of motion (TTHM) and solved them in parallel with the usual hydrodynamic (HDM) equations. Since our TTHM model is parton-based and lacks a description of hadronization, we decided to compare the two approaches just before the onset of hadronization. To make phenomenologically meaningful comparisons we used a HDM reference which had previously been shown to yield a good description of RHIC data when allowed to evolve until hadron freeze-out.

The TTHM turns out to have an extremely stiff equation of state, $P_\perp = \frac{1}{2}\varepsilon$, which causes severe phenomenological problems: in order to avoid the creation of too much radial transverse flow, which would render the single-particle spectra much flatter than observed, while preserving the total multiplicity, we had to start the TTHM evolution very late, at already quite low energy densities. This implies a very long transverse thermaliza-

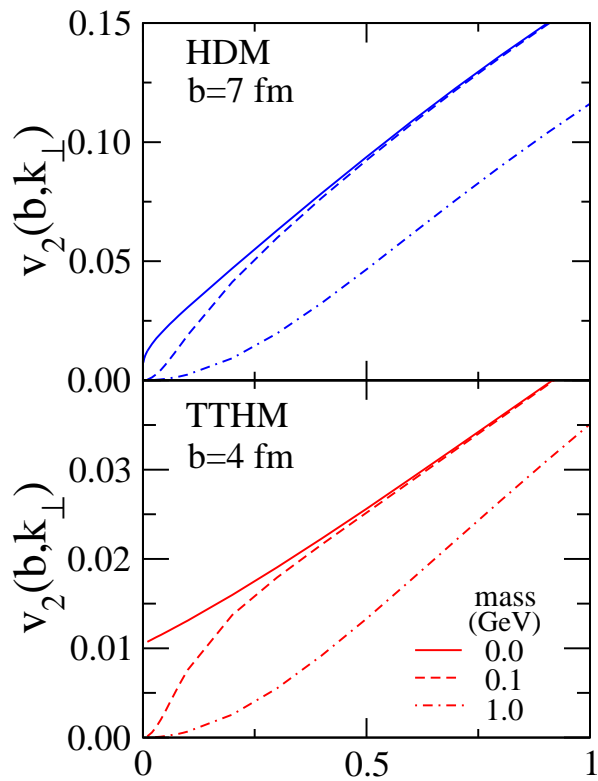


FIG. 10: v_2 as a function of k_\perp for massless and massive bosons from the two models. The solid lines are for massless bosons while the dashed and dot-dashed lines are for bosons with $m=100$ MeV and $m=1$ GeV, respectively.

tion time scale (and, of course, an even longer longitudinal one). While this cannot a priori be excluded theoretically, it causes consistency problems with our implementation which assumes that transverse collective dynamics sets in only after we start the TTHM evolution (i.e. only after thermalization). This is not realistic: even before complete thermalization of the transverse momenta the system will start to evolve in the transverse directions, since nothing confines it. This pre-equilibrium transverse dynamics will likely have a collective component affecting the transverse momentum spectra, necessitating an even further shift of the starting point for TTHM evolution.

We have not followed this issue any further, since there is also a severe problem when comparing the TTHM predictions with the elliptic flow data, which in our opinion eliminates it as a viable model. For the same radial flow, constrained by the slope of the single-particle spectra, TTHM provides only about half as much elliptic flow as the hydrodynamical model and thus significantly less than that required by the RHIC data [1, 2, 3, 8]. This is the central result from the present study, and it strengthens the previously made argument [6, 11] that the large

elliptic flow measured at RHIC can only be reproduced by models which assume very rapid thermalization of the momentum spectra *in all three dimensions*. Partial thermalization, such as the effectively only two-dimensional thermalization in the TTHM model, is not enough to generate the observed elliptic flow. This leaves us with the continued challenge of identifying the microscopic mechanisms within QCD which can cause such rapid three-dimensional thermalization.

Acknowledgements

S.W. thanks Peter Kolb for the FORTRAN code for calculating the nuclear overlap function which was used to initialize the TTHM time evolution. This work was supported by the U.S. Department of Energy under Contract No. DE-FG02-01ER41190.

APPENDIX A: DECOMPOSING THE ENERGY-MOMENTUM TENSOR

To calculate the coefficients in the decomposition (2.19) of the energy-momentum tensor we find it easiest to use the form (2.12) for the distribution function in Eq. (2.18). Assuming massless particles (gluons), we write the four-vector k^μ as

$$k^\mu = k_\perp (\cosh y, \cos \phi, \sin \phi, \sinh y). \quad (\text{A1})$$

We integrate over $d^3k/k_0 = dy k_\perp dk_\perp d\phi$ in Eq. (2.18) by first doing the trivial η -integration and then integrating over k_\perp . After integration over η the exponent of the Bose factor in Eq. (2.12) reduces to

$$\frac{k \cdot u}{T} = \frac{\gamma_\perp k_\perp}{T} (1 - \hat{\mathbf{k}}_\perp \cdot \mathbf{v}_\perp) = \frac{\gamma_\perp k_\perp}{T} (1 - v_\perp \cos(\phi - \phi_s)) \quad (\text{A2})$$

where $\phi - \phi_s$ is the angle between \mathbf{k}_\perp (azimuthal angle ϕ) and \mathbf{v}_\perp (azimuthal angle ϕ_s). The k_\perp -integration is then easily done using

$$\int_0^\infty \frac{k_\perp^n dk_\perp}{e^{\alpha k_\perp} - 1} = \frac{n! \zeta(n+1)}{\alpha^{n+1}}. \quad (\text{A3})$$

In our case $\alpha = \gamma_\perp (1 - v_\perp \cos(\phi - \phi_s))/T$ and $n=3$, and the relevant zeta function is $\zeta(4) = \pi^4/90$. In this way we arrive at

$$T^{\mu\nu} = \frac{\tau_0}{\tau} \frac{\nu}{\gamma_\perp^5} \frac{\pi^2 T^4}{60} \int_{-\pi}^{\pi} \frac{d\phi}{2\pi} \frac{M^{\mu\nu}}{(1 - v_\perp \cos(\phi - \phi_s))^4} \quad (\text{A4})$$

with

$$M^{\mu\nu} = \begin{pmatrix} \cosh^2 \eta & \cos \phi \cosh \eta & \sin \phi \cosh \eta & \cosh \eta \sinh \eta \\ \cos \phi \cosh \eta & \cos^2 \phi & \cos \phi \sin \phi & \cos \phi \sinh \eta \\ \sin \phi \cosh \eta & \cos \phi \sin \phi & \sin^2 \phi & \sin \phi \sinh \eta \\ \cosh \eta \sinh \eta & \cos \phi \sinh \eta & \sin \phi \sinh \eta & \sinh^2 \eta \end{pmatrix}. \quad (\text{A5})$$

The remaining azimuthal integration is done by shifting the integration variable to $\theta = \phi - \phi_s$, using

$$\cos \phi = \cos \theta \cos \phi_s - \sin \theta \sin \phi_s, \quad \sin \phi = \sin \theta \cos \phi_s + \cos \theta \sin \phi_s \quad (\text{A6})$$

in the numerator $M^{\mu\nu}$, and exploiting the formula

$$\int_{-\pi}^{\pi} \frac{d\theta}{2\pi} \frac{1}{(1-v_{\perp} \cos \theta)^n} = \frac{1}{(1-v_{\perp}^2)^{n/2}} P_{n-1} \left(\frac{1}{\sqrt{1-v_{\perp}^2}} \right) = \gamma_{\perp}^n P_{n-1}(\gamma_{\perp}), \quad (\text{A7})$$

where the P_n are Legendre polynomials. We need

$$\gamma_{\perp}^2 P_1(\gamma_{\perp}) = \gamma_{\perp}^3, \quad \gamma_{\perp}^3 P_2(\gamma_{\perp}) = \gamma_{\perp}^5 \left(1 + \frac{1}{2} v_{\perp}^2\right), \quad \gamma_{\perp}^4 P_3(\gamma_{\perp}) = \gamma_{\perp}^7 \left(1 + \frac{3}{2} v_{\perp}^2\right). \quad (\text{A8})$$

M^{00} , $M^{03} = M^{30}$, and M^{33} have no ϕ -dependence and the corresponding angular integrals thus give

$$\int_{-\pi}^{\pi} \frac{d\phi}{2\pi} \frac{1}{(1-v_{\perp} \cos(\phi - \phi_s))^4} = \int_{-\pi}^{\pi} \frac{d\theta}{2\pi} \frac{1}{(1-v_{\perp} \cos \theta)^4} = \gamma_{\perp}^4 P_3(\gamma_{\perp}) = \gamma_{\perp}^7 \left(1 + \frac{3}{2} v_{\perp}^2\right). \quad (\text{A9})$$

For $M^{01} = M^{10}$ and $M^{13} = M^{31}$ we need

$$\begin{aligned} \int_{-\pi}^{\pi} \frac{d\phi}{2\pi} \frac{\cos \phi}{(1-v_{\perp} \cos(\phi - \phi_s))^4} &= \int_{-\pi}^{\pi} \frac{d\theta}{2\pi} \frac{\cos \theta \cos \phi_s - \sin \theta \sin \phi_s}{(1-v_{\perp} \cos \theta)^4} = \frac{\cos \phi_s}{v_{\perp}} \int_{-\pi}^{\pi} \frac{d\theta}{2\pi} \frac{1 - (1-v_{\perp} \cos \theta)}{(1-v_{\perp} \cos \theta)^4} \\ &= \frac{v_x}{v_{\perp}^2} \left(\gamma_{\perp}^4 P_3(\gamma_{\perp}) - \gamma_{\perp}^3 P_2(\gamma_{\perp}) \right) = \frac{1}{2} \gamma_{\perp}^7 v_x (4 + v_{\perp}^2). \end{aligned} \quad (\text{A10})$$

In the last step on the first line we dropped the vanishing term $\sim \sin \theta$ and also added and subtracted a term $1/v_{\perp}$ in the numerator. In the second line we used $\cos \phi_s = v_x/v_{\perp}$. For the remaining components we proceed similarly. The energy-momentum tensor thus takes the form

$$T^{\mu\nu} = \frac{\tau_0}{\tau} \nu_g \frac{\pi^2 T^4}{60} \gamma_{\perp}^2 \begin{pmatrix} (1 + \frac{3}{2} v_{\perp}^2) \cosh^2 \eta & \frac{1}{2} v_x (4 + v_{\perp}^2) \cosh \eta & \frac{1}{2} v_y (4 + v_{\perp}^2) \cosh \eta & (1 + \frac{3}{2} v_{\perp}^2) \cosh \eta \sinh \eta \\ \frac{1}{2} v_x (4 + v_{\perp}^2) \cosh \eta & \frac{1}{2} (1 + 4v_x^2 - v_y^2) & \frac{5}{2} v_x v_y & \frac{1}{2} v_x (4 + v_{\perp}^2) \sinh \eta \\ \frac{1}{2} v_y (4 + v_{\perp}^2) \cosh \eta & \frac{5}{2} v_x v_y & \frac{1}{2} (1 - v_x^2 + 4v_y^2) & \frac{1}{2} v_y (4 + v_{\perp}^2) \sinh \eta \\ (1 + \frac{3}{2} v_{\perp}^2) \cosh \eta \sinh \eta & \frac{1}{2} v_x (4 + v_{\perp}^2) \cosh \eta & \frac{1}{2} v_y (4 + v_{\perp}^2) \sinh \eta & (1 + \frac{3}{2} v_{\perp}^2) \sinh^2 \eta \end{pmatrix}.$$

Contracting this result once with each of the vectors u^{μ} , n^{μ} , and m^{μ} we obtain

$$T^{\mu\nu} u_{\nu} = \frac{\tau_0}{\tau} \nu_g \frac{\pi^2 T^4}{60} \gamma_{\perp}^3 \begin{pmatrix} (1 - \frac{1}{2} v_{\perp}^2 - \frac{1}{2} v_{\perp}^4) \cosh \eta \\ \frac{3}{2} v_x (1 - v_{\perp}^2) \\ \frac{3}{2} v_y (1 - v_{\perp}^2) \\ (1 - \frac{1}{2} v_{\perp}^2 - \frac{1}{2} v_{\perp}^4) \sinh \eta \end{pmatrix}, \quad T^{\mu\nu} m_{\nu} = -\frac{\tau_0}{\tau} \nu_g \frac{\pi^2 T^4}{60} \gamma_{\perp}^3 \begin{pmatrix} (1 - v_{\perp}^2) v_{\perp} \cosh \eta \\ v_x (1 - v_{\perp}^4) / 2 v_{\perp} \\ v_y (1 - v_{\perp}^4) / 2 v_{\perp} \\ (1 - v_{\perp}^2) v_{\perp} \sinh \eta \end{pmatrix}, \quad T^{\mu\nu} n_{\nu} = 0.$$

A second contraction then yields the coefficients A through H in Eq. (2.19) as given in equations (2.22)-(2.27).

APPENDIX B: THE SMALL TRANSVERSE MOMENTUM LIMIT OF ELLIPTIC FLOW

In this Appendix we derive the small- k_{\perp} limit of the elliptic flow coefficient v_2 for TTHM and HDM, for massive and massless particles. Suppressing the impact parameter dependence which is irrelevant here, we write

Eq. (5.6) in the form

$$v_2(k_{\perp}) = \frac{\mathcal{N}}{\mathcal{D}}, \quad (\text{B1})$$

where the numerator \mathcal{N} and denominator \mathcal{D} are obtained from the Cooper-Frye formula (5.1). For massive particles we must generalize Eq. (5.3) by writing the first term as $m_{\perp} \cosh(y-\eta)$ and use

$$k \cdot u = \gamma_{\perp} (m_{\perp} \cosh(y-\eta) - \mathbf{k}_{\perp} \cdot \mathbf{v}_{\perp}). \quad (\text{B2})$$

For the TTHM the distribution function is given by Eq. (2.12), and we obtain for particles at midrapidity $y=0$

$$\left\{ \begin{array}{l} \mathcal{N} \\ \mathcal{D} \end{array} \right\} = \frac{\nu_g \tau_0}{(2\pi)^2} \int \frac{d^2 x_\perp}{\gamma_\perp} \int_{-\infty}^{\infty} d\eta \delta(\eta) \left\{ \begin{array}{l} \mathcal{N}_\phi \\ \mathcal{D}_\phi \end{array} \right\}, \quad (\text{B3})$$

where

$$\left\{ \begin{array}{l} \mathcal{N}_\phi \\ \mathcal{D}_\phi \end{array} \right\} = \int_{-\pi}^{\pi} \frac{d\phi}{2\pi} \left\{ \begin{array}{l} \cos(2\phi) \\ 1 \end{array} \right\} \frac{m_\perp \cosh \eta - \mathbf{k}_\perp \cdot \nabla_\perp \tau_f}{e^{\gamma_\perp (m_\perp \cosh \eta - \mathbf{k}_\perp \cdot \mathbf{v}_\perp) / T - 1}}. \quad (\text{B4})$$

Here γ_\perp and τ_f are functions of the position in the transverse plane, $\gamma_\perp = \gamma_\perp(\mathbf{x}_\perp)$ and $\tau_f = \tau_f(\mathbf{x}_\perp)$. For the HDM we instead use Eq. (3.1) and get

$$\left\{ \begin{array}{l} \mathcal{N} \\ \mathcal{D} \end{array} \right\} = \frac{\nu_g}{(2\pi)^2} \int d^2 x_\perp \tau_f \int_{-\infty}^{\infty} d\eta \left\{ \begin{array}{l} \mathcal{N}_\phi \\ \mathcal{D}_\phi \end{array} \right\}. \quad (\text{B5})$$

The main difference (except for the different weighting of the integration over the transverse plane $d^2 x_\perp = r dr d\phi_s$) is the nontrivial η -integration in the HDM case.

1. Massive particles: For non-zero rest mass, $m \neq 0$, we can expand in both cases the ϕ -integrand for small k_\perp . Keeping only terms up to first order in k_\perp we find

$$\left\{ \begin{array}{l} \mathcal{N}_\phi \\ \mathcal{D}_\phi \end{array} \right\} \approx \frac{m \cosh \eta}{e^{\gamma_\perp m \cosh \eta / T} - 1} \int_{-\pi}^{\pi} \frac{d\phi}{2\pi} \left\{ \begin{array}{l} \cos(2\phi) \\ 1 \end{array} \right\} \quad (\text{B6})$$

$$\times \left(1 - \frac{\mathbf{k}_\perp \cdot \nabla_\perp \tau_f}{m \cosh \eta} \right) \left(1 + \frac{\mathbf{k}_\perp \cdot \mathbf{v}_\perp}{T} \frac{\gamma_\perp}{1 - e^{-\gamma_\perp m \cosh \eta / T}} \right).$$

Higher orders of k_\perp come with higher inverse powers of T or $m \cosh \eta$; the corresponding η -integrals thus are all finite (trivially so in the TTHM), and the k_\perp -expansion is well-behaved.

As in Appendix A we write $\mathbf{k}_\perp \cdot \mathbf{v}_\perp = k_\perp v_\perp \cos(\phi - \phi_s) \equiv k_\perp v_\perp \cos \theta$ and use $-\pi \leq \theta \leq \pi$ as integration variable. Then, using Eq. (A6),

$$\hat{\mathbf{k}}_\perp \cdot \nabla_\perp \tau_f = (\partial_r \tau_f) \cos \theta + (\partial_\phi \tau_f) \sin \theta, \quad (\text{B7})$$

where $\partial_r \tau_f = \hat{\mathbf{v}}_\perp \cdot \nabla_\perp \tau_f$ and $\partial_\phi \tau_f = \hat{\mathbf{z}} \cdot (\hat{\mathbf{v}}_\perp \times \nabla_\perp \tau_f)$. Here $\hat{\mathbf{z}}$ is the unit vector along the beam direction, and $\hat{\mathbf{v}}_\perp$ coincides with the radial unit vector, $\hat{\mathbf{v}}_\perp = (\cos \phi_s, \sin \phi_s)$. We also need

$$\begin{aligned} \cos(2\phi) &= \cos(2\phi_s)(\cos^2 \theta - \sin^2 \theta) \\ &\quad - 2 \sin(2\phi_s) \sin \theta \cos \theta. \end{aligned} \quad (\text{B8})$$

After these manipulations the angular integrations in Eq. (B6) are easily performed. Due to symmetric integration over the full circle, only terms containing even powers of $\cos \theta$ and/or $\sin \theta$ survive. We find

$$\mathcal{N}_\phi = \mathcal{O}(k_\perp^2), \quad \mathcal{D}_\phi = a + b k_\perp + \mathcal{O}(k_\perp^2), \quad (\text{B9})$$

where a and b are integrable functions of \mathbf{x}_\perp and η . As a result, for massive particles $v_2(k_\perp) = \mathcal{O}(k_\perp^2)$, i.e. the elliptic flow coefficient vanishes with zero slope when $k_\perp \rightarrow 0$, as first observed by Danielewicz [19].

2. Massless bosons in the TTHM: For massless bosons at $y=0$ the angular integrals $\mathcal{N}_\phi, \mathcal{D}_\phi$ in Eq. (B4) reduce to

$$\left\{ \begin{array}{l} \mathcal{N}_\phi \\ \mathcal{D}_\phi \end{array} \right\} = \frac{T}{\gamma_\perp} \int_{-\pi}^{\pi} \frac{d\phi}{2\pi} \left\{ \begin{array}{l} \cos(2\phi) \\ 1 \end{array} \right\} \frac{1 - \frac{\hat{\mathbf{k}}_\perp \cdot \nabla_\perp \tau_f}{\cosh \eta}}{1 - \frac{\hat{\mathbf{k}}_\perp \cdot \mathbf{v}_\perp}{\cosh \eta}}$$

$$\times \frac{\frac{\gamma_\perp k_\perp}{T} (\cosh \eta - \hat{\mathbf{k}}_\perp \cdot \mathbf{v}_\perp)}{e^{\frac{\gamma_\perp k_\perp}{T} (\cosh \eta - \hat{\mathbf{k}}_\perp \cdot \mathbf{v}_\perp)} - 1}. \quad (\text{B10})$$

We can try to expand the last factor for small k_\perp by using

$$\frac{x}{e^x - 1} = 1 - \frac{x}{2} + \mathcal{O}(x^2). \quad (\text{B11})$$

However, since in this expression the expansion parameter is $x = \frac{\gamma_\perp k_\perp}{T} (\cosh \eta - \hat{\mathbf{k}}_\perp \cdot \mathbf{v}_\perp)$, each additional power of k_\perp brings in another factor $\cosh \eta$. This is no problem for the TTHM with its factor $\delta(\eta)$ under the η -integral, but for the HDM the η -integrals of the expansion coefficients diverge, rendering the expansion meaningless. For the HDM thus the η -integration must be performed *before* we expand for small k_\perp (see **3.** below).

For the TTHM, on the other hand, we can continue along this direction. Using the same manipulations as in **1.** above, we find up to linear order in k_\perp

$$\left\{ \begin{array}{l} \mathcal{N}_\phi \\ \mathcal{D}_\phi \end{array} \right\} \approx \frac{T}{\gamma_\perp} \int_{-\pi}^{\pi} \frac{d\theta}{2\pi} \left\{ \begin{array}{l} \cos(2\phi_s) \cos(2\theta) - \sin(2\phi_s) \sin(2\theta) \\ 1 \end{array} \right\}$$

$$\times \frac{1 - (\partial_r \tau_f) \cos \theta - (\partial_\phi \tau_f) \sin \theta}{1 - v_\perp \cos \theta}$$

$$\times \left(1 - \frac{\gamma_\perp k_\perp}{2T} (1 - v_\perp \cos \theta) \right). \quad (\text{B12})$$

We use Eq. (A7) to derive the following table of integrals:

$$\begin{aligned} \int_{-\pi}^{\pi} \frac{d\theta}{2\pi} \frac{1}{1 - v_\perp \cos \theta} &= \gamma_\perp, \\ \int_{-\pi}^{\pi} \frac{d\theta}{2\pi} \frac{\cos \theta}{1 - v_\perp \cos \theta} &= \frac{\gamma_\perp - 1}{v_\perp}, \\ \int_{-\pi}^{\pi} \frac{d\theta}{2\pi} \frac{\cos^2 \theta}{1 - v_\perp \cos \theta} &= \frac{\gamma_\perp - 1}{v_\perp^2}, \\ \int_{-\pi}^{\pi} \frac{d\theta}{2\pi} \frac{\sin^2 \theta}{1 - v_\perp \cos \theta} &= \frac{\gamma_\perp - 1}{\gamma_\perp v_\perp^2}, \\ \int_{-\pi}^{\pi} \frac{d\theta}{2\pi} \frac{\cos(2\theta)}{1 - v_\perp \cos \theta} &= \frac{1}{\gamma_\perp} \left(\frac{\gamma_\perp - 1}{v_\perp} \right)^2, \\ \int_{-\pi}^{\pi} \frac{d\theta}{2\pi} \frac{\sin^2 \theta \cos \theta}{1 - v_\perp \cos \theta} &= \frac{1}{2v_\perp} \left(\frac{\gamma_\perp - 1}{\gamma_\perp v_\perp} \right)^2, \\ \int_{-\pi}^{\pi} \frac{d\theta}{2\pi} \frac{\cos(2\theta) \cos \theta}{1 - v_\perp \cos \theta} &= \frac{1}{\gamma_\perp v_\perp} \left(\frac{\gamma_\perp - 1}{v_\perp} \right)^2, \end{aligned} \quad (\text{B13})$$

and find

$$\begin{aligned}\mathcal{N}_\phi &= T \left(\frac{\gamma_\perp - 1}{\gamma_\perp v_\perp} \right)^2 \left[\cos(2\phi_s) \left(1 - \frac{\partial_r \tau_f}{v_\perp} \right) \right. \\ &\quad \left. + \sin(2\phi_s) \frac{\partial_\phi \tau_f}{\gamma_\perp v_\perp} \right] + \mathcal{O}(k_\perp^2), \\ \mathcal{D}_\phi &= T \left(1 - \frac{\gamma_\perp - 1}{\gamma_\perp v_\perp} (\partial_r \tau_f) \right) - \frac{k_\perp}{2} + \mathcal{O}(k_\perp^2).\end{aligned}\quad (\text{B14})$$

Now both the numerator and denominator approach nonzero constants as $k_\perp \rightarrow 0$. Since the fireball center freezes out later than its edge, the term $\sim (\partial_r \tau_f)$, after integration over the transverse plane, contributes with a negative sign, and the k_\perp -independent first terms in \mathcal{N}_ϕ and \mathcal{D}_ϕ are correspondingly positive. As a result, the small- k_\perp expansion of the elliptic flow coefficient takes the form

$$\begin{aligned}v_2(k_\perp) &= \frac{\mathcal{N}}{\mathcal{D}} = \frac{a}{1 - bk_\perp} + \mathcal{O}(k_\perp^2) \\ &= a + abk_\perp + \mathcal{O}(k_\perp^2),\end{aligned}\quad (\text{B15})$$

where a and b are positive constants arising from the integration over the transverse profiles of the freeze-out time and flow velocity. Thus, as $k_\perp \rightarrow 0$, v_2 approaches a positive constant value with nonzero positive slope, as confirmed by Figs. 7 to 9.

3. Massless bosons from the HDM: In the last step we discuss the corresponding limit for massless bosons from the HDM, in order to understand the surprising behaviour shown in the upper part of Fig. 9. As already mentioned, in this case the η -integration must be performed *before* expanding in k_\perp . Doing this integration first, we rewrite Eq. (B5) as

$$\begin{aligned}\left\{ \frac{\mathcal{N}}{\mathcal{D}} \right\} &= \frac{\nu_g}{(2\pi)^2} \int r dr d\phi_s \frac{\tau_f(r, \phi_s)}{\gamma_\perp(r, \phi_s)} \\ &\quad \times \int_{-\pi}^{\pi} \frac{d\theta}{2\pi} \left\{ \frac{\cos(2\phi_s) \cos(2\theta) - \sin(2\phi_s) \sin(2\theta)}{1} \right\} \\ &\quad \times \int_{-\infty}^{\infty} d\eta \frac{\xi \left(\cosh \eta - \hat{\mathbf{k}}_\perp \cdot \nabla_\perp \tau_f \right)}{e^{\xi(\cosh \eta - \hat{\mathbf{k}}_\perp \cdot \mathbf{v}_\perp)} - 1},\end{aligned}\quad (\text{B16})$$

where all the dependence on the magnitude of k_\perp is hidden in the variable

$$\xi = \frac{\gamma_\perp k_\perp}{T}.\quad (\text{B17})$$

Let us denote the result of the η -integral by I_η . Expanding the Bose-Einstein distribution in a power series and performing the η -integration term by term we find

$$\begin{aligned}I_\eta &= \xi \sum_{n=1}^{\infty} e^{nv_\perp \xi \cos \theta} \int_{-\infty}^{\infty} d\eta e^{-n\xi \cosh \eta} \\ &\quad \times (\cosh \eta - (\partial_r \tau_f) \cos \theta - (\partial_\phi \tau_f) \sin \theta) \\ &= 2\xi \sum_{n=1}^{\infty} e^{nv_\perp \xi \cos \theta} \left[\text{K}_1(n\xi) \right. \\ &\quad \left. - (\cos \theta (\partial_r \tau_f) + \sin \theta (\partial_\phi \tau_f)) \text{K}_0(n\xi) \right],\end{aligned}\quad (\text{B18})$$

where the K_ν are modified Bessel functions of the second kind. The integration over the momentum-space angle θ can now be performed, too, yielding modified Bessel functions of the first kind I_ν :

$$\int_{-\pi}^{\pi} \frac{d\theta}{2\pi} \cos(\nu\theta) e^{z \cos \theta} = \text{I}_\nu(z),\quad (\text{B19})$$

where $z = nv_\perp \xi$. After some simple manipulations using trigonometric identities we find for the elliptic flow coefficient

$$v_2(k_\perp) = \frac{\sum_{n=1}^{\infty} \int r dr d\phi_s \frac{\tau_f(r, \phi_s)}{\gamma_\perp(r, \phi_s)} \mathcal{N}_n(r, \phi_s; k_\perp)}{\sum_{n=1}^{\infty} \int r dr d\phi_s \frac{\tau_f(r, \phi_s)}{\gamma_\perp(r, \phi_s)} \mathcal{D}_n(r, \phi_s; k_\perp)},\quad (\text{B20})$$

where

$$\begin{aligned}\mathcal{N}_n &= \cos(2\phi_s) \left[\xi \text{I}_2(nv_\perp \xi) \text{K}_1(n\xi) \right. \\ &\quad \left. - \frac{\partial_r \tau_f}{2} \xi \left(\text{I}_1(nv_\perp \xi) + \text{I}_3(nv_\perp \xi) \right) \text{K}_0(n\xi) \right] \\ &\quad + \sin(2\phi_s) \frac{\partial_\phi \tau_f}{2} \xi \left(\text{I}_1(nv_\perp \xi) - \text{I}_3(nv_\perp \xi) \right) \text{K}_0(n\xi), \\ \mathcal{D}_n &= \xi \text{I}_0(nv_\perp \xi) \text{K}_1(n\xi) - (\partial_r \tau_f) \xi \text{I}_1(nv_\perp \xi) \text{K}_0(n\xi).\end{aligned}\quad (\text{B21})$$

These expressions generalize the result given in [7] to the general case of a freeze-out time τ_f which depends on the transverse position \mathbf{x}_\perp .

We can now study the small-momentum limit of v_2 by letting $\xi \rightarrow 0$. Let us first consider the Boltzmann approximation which corresponds to keeping only the terms \mathcal{N}_1 and \mathcal{D}_1 in Eq. (B20). Using the small- ξ expansions of the Bessel functions one finds that in this approximation

$$\lim_{k_\perp \rightarrow 0} v_2^{\text{Boltz}}(k_\perp) \sim \frac{k_\perp^2}{T^2} \ln \frac{k_\perp}{T}.\quad (\text{B22})$$

For massless Boltzmann particles, the elliptic flow from the HDM thus goes to zero with zero slope, but by a factor $\ln(k_\perp/T)$ more slowly than for massive particles, see point **1.** above.

For bosons we must sum over all n in Eq. (B20). For $k_\perp \rightarrow 0$, i.e. $\xi \rightarrow 0$, the sum over n becomes the discrete representation of an integral: defining

$$f_{v_\perp}(\zeta) \equiv \text{I}_\nu(v_\perp \zeta) \text{K}_\mu(\zeta),\quad (\text{B23})$$

we have

$$\begin{aligned}\xi \sum_{n=1}^{\infty} \text{I}_\nu(nv_\perp \zeta) \text{K}_\mu(n\xi) &= \xi \sum_{n=1}^{\infty} f_{v_\perp}(n\xi) \\ &\longrightarrow \int_{\xi/2}^{\infty} f_{v_\perp}(\zeta) d\zeta.\end{aligned}\quad (\text{B24})$$

By expanding the Bessel functions for large arguments one sees that for large ζ

$$f_{v_\perp}(\zeta) \approx \frac{1}{2\sqrt{v_\perp \zeta}} e^{-(1-v_\perp)\zeta},\quad (\text{B25})$$

such that the integral in Eq. (B24) clearly converges at the upper end. The k_{\perp} -dependence of v_2 can now be extracted by studying the dependence of this integral on its lower limit $\xi/2 = \gamma_{\perp} k_{\perp}/2T$. To do so we employ the following trick: We split the integral at an arbitrary intermediate scale λ ,

$$\begin{aligned} \int_{\xi/2}^{\infty} f_{v_{\perp}}(\zeta) d\zeta &= \int_{\xi/2}^{\lambda} f_{v_{\perp}}(\zeta) d\zeta + \int_{\lambda}^{\infty} f_{v_{\perp}}(\zeta) d\zeta \\ &= \int_{\xi/2}^{\lambda} f_{v_{\perp}}(\zeta) d\zeta + F(\lambda; v_{\perp}), \end{aligned} \quad (\text{B26})$$

where $F(\lambda; v_{\perp})$ is a finite number whose dependence on λ cancels against the λ -dependence of the first integral, irrespective of how we choose λ . By taking $\xi/2 < \lambda \ll 1$ we can evaluate the first integral analytically by making use of the expansion of the Bessel functions for small arguments, keeping only the leading terms. In the limit $\xi \rightarrow 0$ we find in this way

$$\int_{\xi/2}^{\lambda} I_2(v_{\perp}\zeta) K_1(\zeta) d\zeta \longrightarrow \frac{\lambda^2 v_{\perp}^2}{16},$$

$$\begin{aligned} \int_{\xi/2}^{\lambda} I_1(v_{\perp}\zeta) K_0(\zeta) d\zeta &\longrightarrow \frac{v_{\perp}}{16} \xi^2 \ln(a\xi) + C(\lambda), \\ \int_{\xi/2}^{\lambda} I_3(v_{\perp}\zeta) K_0(\zeta) d\zeta &\longrightarrow 0, \\ \int_{\xi/2}^{\lambda} I_0(v_{\perp}\zeta) K_1(\zeta) d\zeta &\longrightarrow \ln \frac{2\lambda}{\xi} + C'(\lambda), \end{aligned} \quad (\text{B27})$$

where a is a λ -independent constant while C, C' depend on λ but combine with the corresponding constants $F(\lambda; v_{\perp})$ to finite, λ -independent constants. Inserting these results into Eqs. (B20) and (B21) we finally obtain

$$\lim_{k_{\perp}/T \rightarrow 0} v_2(k_{\perp}) = \frac{\text{const.}}{\ln \frac{T}{k_{\perp}}}, \quad (\text{B28})$$

which approaches zero with infinite slope. This is exactly the behaviour seen in the upper panel of Fig. 9 for massless bosons.

-
- [1] K.H. Ackermann *et al.*, STAR Collaboration, Phys. Rev. Lett. **86**, 402 (2001).
[2] C. Adler *et al.*, STAR Collaboration, Phys. Rev. Lett. **87**, 182301 (2001).
[3] R. Snellings for the STAR Collaboration, Nucl. Phys. A **698**, 193c (2002).
[4] J.Y. Ollitrault, Phys. Rev. D **46**, 229 (1992).
[5] P.F. Kolb, J. Sollfrank, and U. Heinz, Phys. Lett. B **459**, 667 (1999); and Phys. Rev. C **62**, 054909 (2000).
[6] P.F. Kolb, P. Huovinen, U. Heinz, and H. Heiselberg, Phys. Lett. B **500**, 232 (2001); P.F. Kolb, U. Heinz, P. Huovinen, K.J. Eskola, and K. Tuominen, Nucl. Phys. A **696**, 197 (2001).
[7] P. Huovinen, P.F. Kolb, U. Heinz, P.V. Ruuskanen, and S.A. Voloshin, Phys. Lett. B **503**, 58 (2001);
[8] R.A. Lacey for the PHENIX Collaboration, Nucl. Phys. A **698**, 559c (2002); K. Adcox *et al.*, PHENIX Collaboration, nucl-ex/0204005.
[9] I.C. Park for the PHOBOS Collaboration, Nucl. Phys. A **698**, 564c (2002).
[10] S. Voloshin and Y. Zhang, Z. Phys. C **70**, 665 (1996).
[11] U. Heinz and P. Kolb, Nucl. Phys. A **702**, 269 (2002); and hep-ph/0204061.
[12] This assumption is not unreasonable because flow anisotropies require anisotropic pressure gradients for building up, but at the same time they reduce the latter dynamically [13]. The necessary spatial transverse anisotropies thus exist only during the very early collision stages, and we here assume that the time needed to eliminate them is shorter than the longitudinal thermalization time.
[13] H. Sorge, Phys. Rev. Lett. **78**, 2309 (1997); *ibid.* **82**, 2048 (1999)
[14] J.D. Bjorken, Phys. Rev. D **27**, 140 (1983).
[15] P.V. Ruuskanen, Acta Phys. Pol. **18**, 551 (1988).
[16] F. Cooper and G. Frye, Phys. Rev. D **10**, 186 (1974).
[17] As shown in Fig. 1 of [18], the equation of state of an ideal massless gluon gas is so stiff that at RHIC energies the fireball freezes out dynamically (i.e. driven by strong transverse flow) before the spatial deformation of the reaction zone in noncentral collisions has fully disappeared. Therefore, with such an equation of state, elliptic flow does not fully saturate before decoupling. Nonetheless, the same Figure shows [18] that more than half of the maximally possible elliptic flow develops before the decoupling energy density is reached.
[18] P. F. Kolb, J. Sollfrank, P. V. Ruuskanen, and U. Heinz, Nucl. Phys. A **661**, 349 (1999).
[19] P. Danielewicz, Phys. Rev. C **51**, 716 (1995).
[20] K. Geiger, Phys. Rep. **258**, 237 (1995).
[21] S.M.H. Wong, Nucl. Phys. A **607**, 442 (1996); Phys. Rev. C **54**, 2588 (1996); Phys. Rev. C **56**, 1075 (1997); Nucl. Phys. A **638**, 527c (1998); Phys. Rev. C **61**, 064903 (2000);
[22] D. Molnar and M. Gyulassy, Nucl. Phys. A **697**, 495 (2002).